ELECTOCTRONIC SUPPLEMENTARY INFORMATION (ESI)

Directed assembly of a high surface area 2D metal-organic framework displaying the augmented "kagomé dual" (kgd-a) layered topology with high H_2 and CO_2 uptake

Ioannis Spanopoulos,[a] Constantinos Tsangarakis,[a] Sarah Barnett,[b] Harriot Nowell,[b] Emmanuel Klontzas,[a] George E. Froudakis[a] and Pantelis N. Trikalitis[a,*]

[a] *Department of Chemistry, University of Crete, Voutes 71003 Heraklion, Greece*

[b] *Diamond Light Source, Harwell Science and Innovation Campus, Didcot, Oxfordshire OX11 0DE, UK*

Table of Contents

Optical images of 1

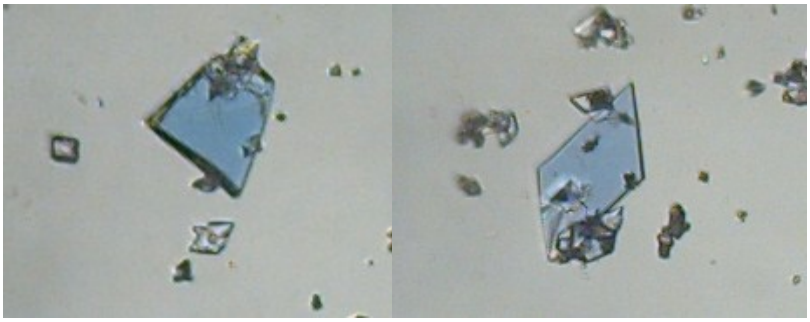

Figure S1. Optical microscope pictures of single crystals of **1.**

Energy Dispersive Spectroscopy Analysis (EDS)

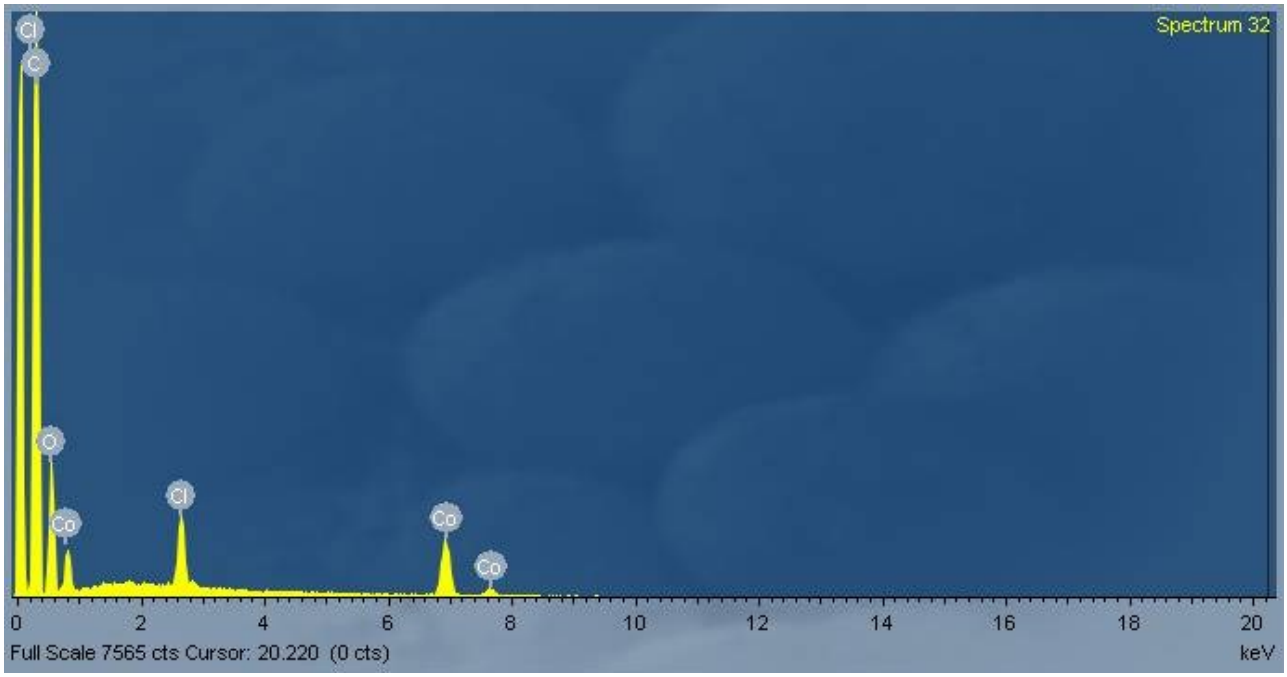

Figure S2. EDS spectrum of **1** obtained in an scanning electron miscroscope.

Table S1. EDS quantitative analysis of **1** on different single crystals.
Crystal #1:

Element	App	Intensity	Weight%	Weight%	**Atomic%**
	Conc.	Corrn.		Sigma	
Cl K	13.90	0.8312	1.78	0.06	**0.68**
Co K	43.06	0.7668	5.98	0.15	**1.38**

Crystal #2:

Element	App	Intensity	Weight%	Weight%	**Atomic%**
	Conc.	Corrn.		Sigma	
Cl K	14.78	0.8312	1.87	0.06	**0.72**
Co K	46.01	0.7675	6.30	0.18	**1.46**

Crystal #3:

Element	App	Intensity	Weight%	Weight%	**Atomic%**
	Conc.	Corrn.		Sigma	
Cl K	14.33	0.8313	1.83	0.06	**0.70**
Co K	43.48	0.7669	6.03	0.15	**1.39**

Single crystal data

Table S2. Crystal data and structure refinement for **1** at 250(2) K.

Empirical formula	C84 H48 Cl2 Co4 O18
Formula weight	1651.84
Temperature	250(2) K
Wavelength	0.6889 Å
Crystal system	Monoclinic
Space group	C2/m
Unit cell dimensions	a = 30.84(3) Å, α = 90º b = 23.83(2) Å, β = 101.531(13)º c = 21.31(2) Å, γ = 90º
Volume	15347(24) $Å^3$
Z	4
Density (calculated)	0.715 g/cm^3
Absorption coefficient	0.495 mm^{-1}
F(000)	3352
Crystal size	0.300 x 0.200 x 0.050 mm^3
Theta range for data collection	1.326 to 26.018º
Index ranges	-38<=h<=38, -30<=k<=30, -26<=l<=27
Reflections collected	114185
Independent reflections	16726 [R_{int} = 0.0810]
Completeness to θ = 24.415º	100%
Refinement method	Full-matrix least-squares on F^2
Data / restraints / parameters	16726 / 24 / 547
Goodness-of-fit on F^2	1.520
Final R indices [I > 2σ(I)]	R_{obs} = 0.1091, wR_{obs} = 0.2860
R indices (all data)	R_{all} = 0.1511, wR_{all} = 0.3063
Largest diff. peak and hole	0.932 and -0.846 $e.Å^{-3}$

$R = \Sigma||F_o|-|F_c|| / \Sigma|F_o|$, $wR = \{\Sigma[w(|F_o|^2 - |F_c|^2)^2] / \Sigma[w(|F_o|^4)]\}^{1/2}$ and $w=1/[\sigma^2(Fo^2)+(0.1000P)^2]$ where $P=(Fo^2+2Fc^2)/3$

Table S3. Selected bond lengths [Å] for **1** at 250(2) K with estimated standard deviations in parentheses.

Label	Distances
Co(1)-O(1)	2.042(3)
Co(1)-O(1)#1	2.042(3)
Co(1)-O(4)#2	2.090(5)
Co(1)-O(9)	2.099(6)
Co(1)-O(10)#1	2.145(4)
Co(1)-O(10)	2.145(4)
Co(2)-O(2)#1	1.944(4)
Co(2)-O(2)	1.944(4)
Co(2)-O(3)#2	2.025(4)
Co(2)-Cl(2)	2.236(3)
Co(2)-O(4)#2	2.391(5)
Co(3)-O(5)	1.915(4)
Co(3)-O(5)#1	1.915(4)
Co(3)-O(8)#3	1.935(5)
Co(3)-Cl(1)	2.225(3)
Co(4)-O(6)	2.002(5)
Co(4)-O(6)#1	2.002(5)
Co(4)-O(7)#3	2.020(7)
Co(4)-O(12)	2.082(8)
Co(4)-O(11)#1	2.172(7)
Co(4)-O(11)	2.172(7)

Symmetry transformations used to generate equivalent atoms:
1# x,-y+1,z 2# -x-1/2,-y+1/2,-z+2 3# -x-1/2,-y+1/2,-z+1

Table S4. Crystal data and structure refinement for **2** at 120(2) K.

Empirical formula	C84 H44 Co2 O14
Formula weight	1395.05
Temperature	120(2) K
Wavelength	0.86380 Å
Crystal system	Monoclinic
Space group	C2/m
Unit cell dimensions	a = 41.909(13) Å, α = 90º b = 24.156(7) Å, β = 95.829(5)º c = 11.898(4) Å, γ = 90º
Volume	11982(6) $Å^3$
Z	4
Density (calculated)	0.773 g/cm^3
Absorption coefficient	0.316 mm^{-1}
F(000)	2856
Crystal size	0.400 x 0.200 x 0.200 mm^3
Theta range for data collection	0.974 to 25.541º
Index ranges	-48<=h<=50, -28<=k<=28, -12<=l<=9
Reflections collected	38635
Independent reflections	9917 [R_{int} = 0.0408]
Completeness to θ = 25.242º	91%
Refinement method	Full-matrix least-squares on F^2
Data / restraints / parameters	9917 / 0 / 451
Goodness-of-fit on F^2	1.201
Final R indices [I > 2σ(I)]	R_{obs} = 0.0680, wR_{obs} = 0.1899
R indices (all data)	R_{all} = 0.0834, wR_{all} = 0.2010
Largest diff. peak and hole	0.574 and -0.557 e.$Å^{-3}$

$R = \Sigma||F_o|-|F_c|| / \Sigma|F_o|$, $wR = \{\Sigma[w(|F_o|^2 - |F_c|^2)^2] / \Sigma[w(|F_o|^4)]\}^{1/2}$ and $w=1/[\sigma^2(Fo^2)+(0.1000P)^2]$ where $P=(Fo^2+2Fc^2)/3$

Table S5. Selected bond lengths [Å] for **2** at 120(2) K with estimated standard deviations in parentheses.

Label	Distances
Co(1)-O(5)	2.000(2)
Co(1)-O(1)	2.047(3)
Co(1)-O(6)	2.062(2)
Co(1)-O(3)	2.073(2)
Co(1)-O(2)	2.326(2)
Co(1)-O(7)	2.393(3)

Powder X-ray diffraction

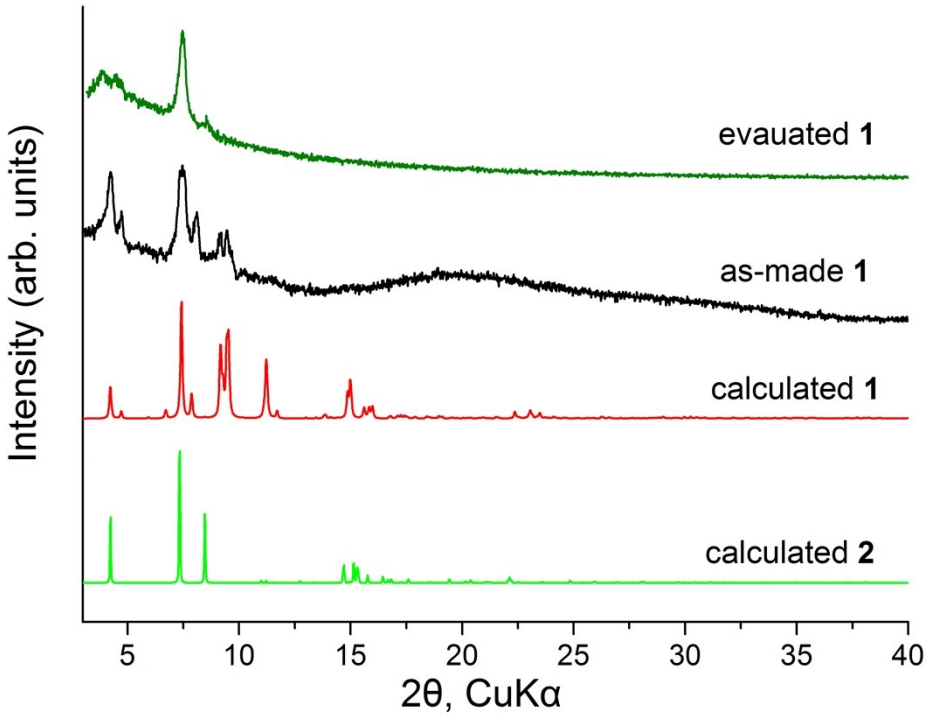

Figure S3. Powder X-ray diffraction pattern of calculated **1** and **2**, as made **1** and evacuated **1**.

Additional gas sorption data and analyses

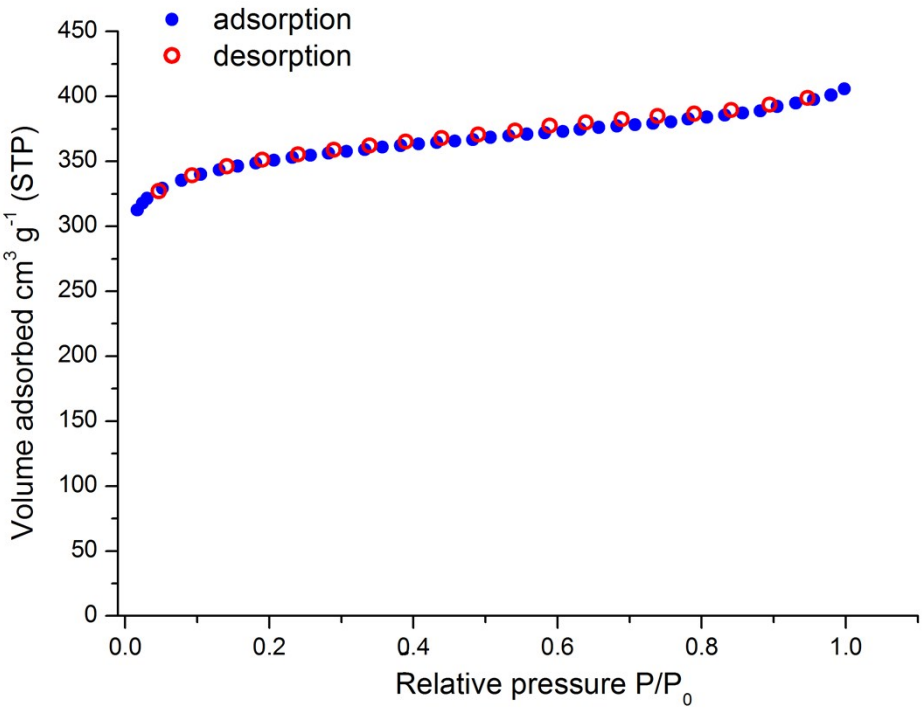

Figure S4. Nitrogen adsorption isotherm of **1** recorded at 77 K.

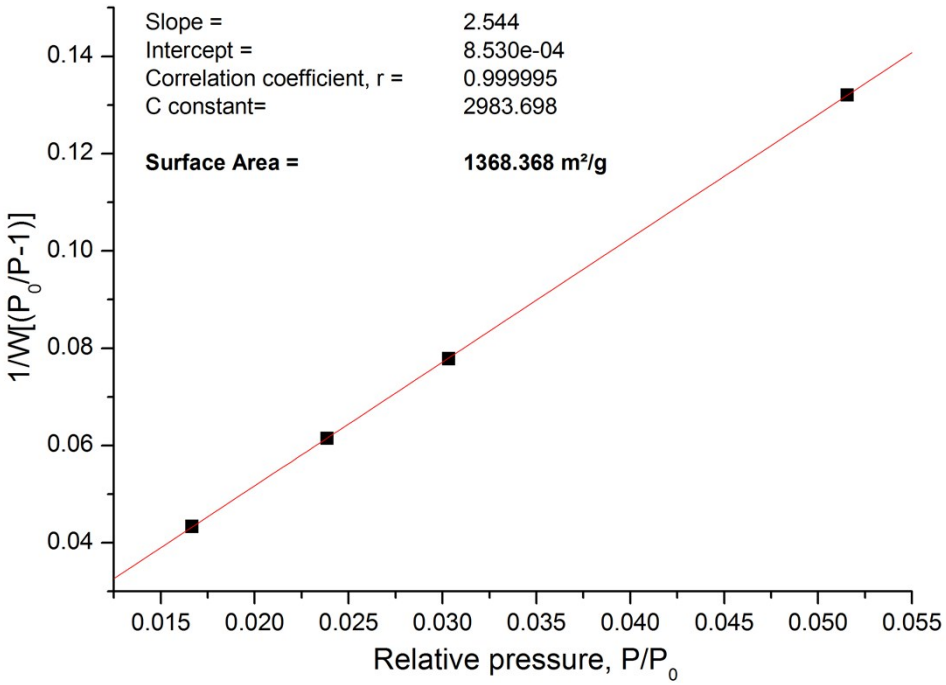

Figure S5. BET plot for **1** from N_2 adsorption isotherm.

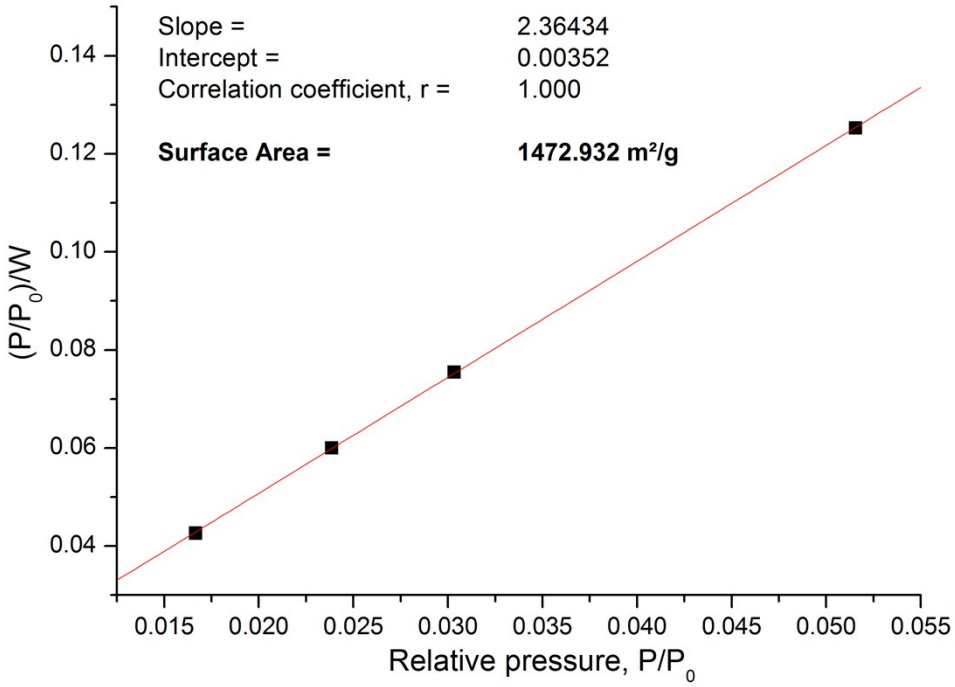

Figure S6. Langmuir plot for **1** from N_2 adsorption isotherm.

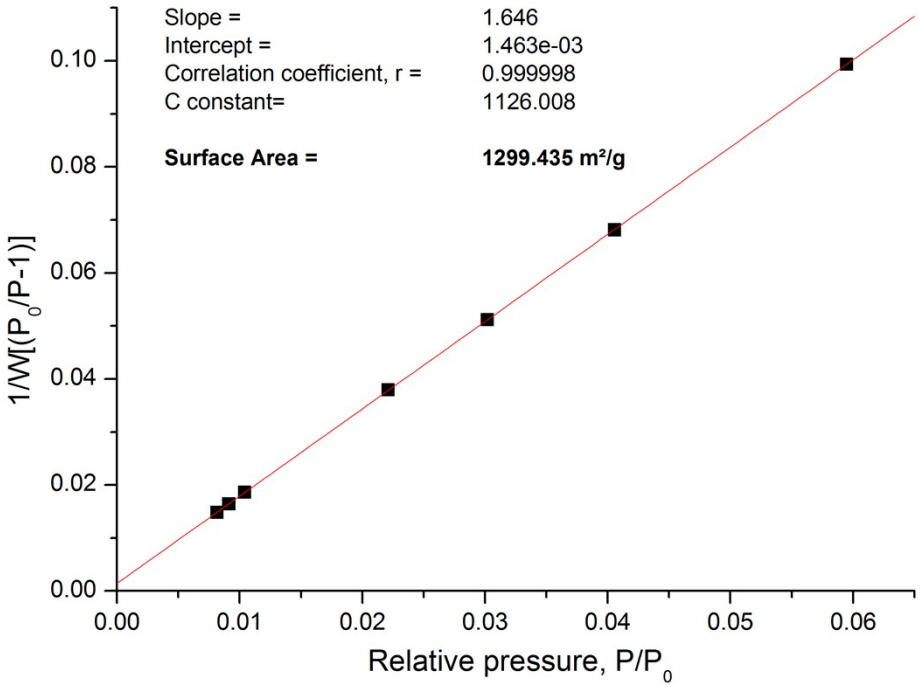

Figure S7. BET plot for **1** from Ar adsorption isotherm.

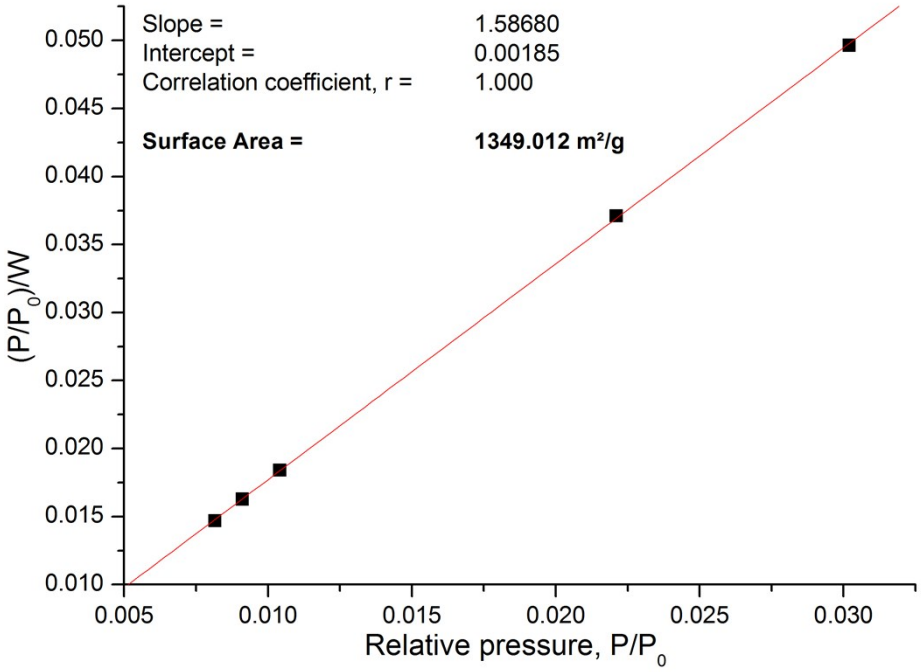

Figure S8. Langmuir plot for **1** from Ar adsorption isotherm.

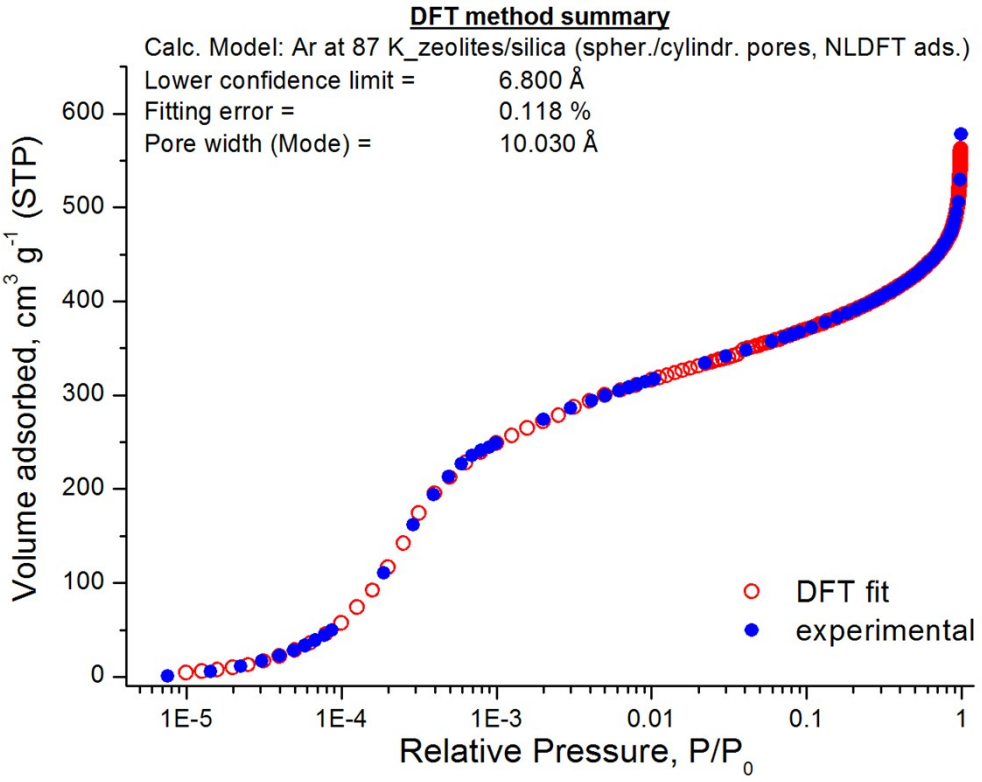

Figure S9. Argon adsorption isotherm of **1** at 87 K in logarithmic scale and the corresponding NLDFT fitting.

Low pressure CO_2, CH_4, and H_2 sorption isotherms, determination of heat of adsorption and CO_2/CH_4 selectivity calculations using IAST.

Heat of adsorption. For the determination of the isosteric heat of adsorption using the Clausious-Clapeyron equation, a commercially available software, ASiQwin (version 3.01) purchased from Quantachrome, was used.

Gas selectivity using IAST. The corresponding calculations were performed according to an established procedure.[1] Specifically, the single-component adsorption isotherms were described by fitting the data with the following virial-type equation:

$$p = \frac{n}{K} exp(c_1 1n + c_2 n^2 + c_3 n^3 + c_4 n^4) \quad (1)$$

where p is the pressure in Torr, n is the adsorbed amount in mmol g^{-1}, K is the Henry constant in mmol g^{-1} $Torr^{-1}$ and c_i are the constants of the virial equation.

The free energy of desorption at a given temperature and pressure of the gas is obtained from the analytical integration of eq. (1):

$$G(T,p) = RT \int_0^p \frac{n}{p} dp = RT(n + \frac{1}{2}c_1 n^2 + \frac{2}{3}c_2 n^3 + \frac{3}{4}c_3 n^4 + \frac{4}{5}c_4 n^5) \quad (2)$$

The free energy of desorption is a function of temperature and pressure *G(T,p)* and describes the minimum work (Gibbs free energy) that required to completely degas the adsorbent surface.

For a binary mixture of component *i* and *j* eq. (2) yields the individual pure loadings n_i^0 and n_j^0 at the same free energy of desorption:

$$G_i^0(n_i^0) = G_j^0(n_j^0) \quad (3)$$

The partial pressure of component *i* and *j* in an ideal adsorption mixture is given by the following equations:

$$py_i = p_i^0(n_i^0)x_i \quad (4)$$

$$py_j = p_j^0(n_j^0)x_j \quad (5)$$

where y_i *(=1-y_j)* and x_i *(=1-x_j)* is the molar fraction of component *i* in the gas phase and the adsorbed phase respectively and p_i^0, p_j^0 is the pure component pressure of *i* and *j* respectively. From eq. (3)-(5), the selectivity for the adsorbates *i* and *j* ($S_{i,j}$) and the total pressure (p) of the gas mixture were calculated from eq. (6) and eq. (7), respectively.

$$S_{ij} = \frac{x_i/y_i}{x_j/y_j} = \frac{p_j^0}{p_i^o} \quad (6)$$

$$p = \sum_i^j (p_i^o x_i) \quad (7)$$

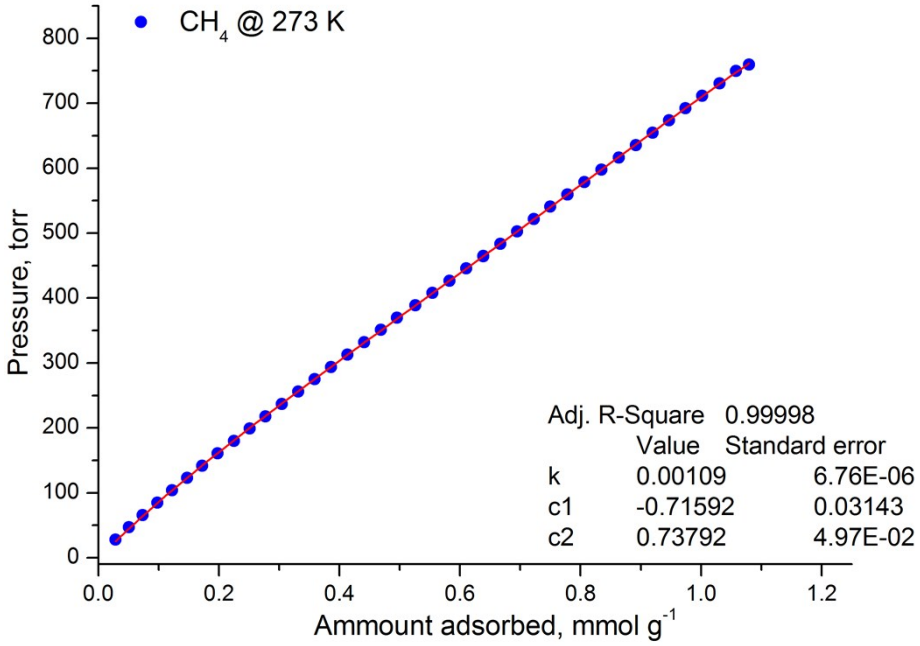

Figure S10. Virial type fitting of CH_4 adsorption isotherms of **1** at 273 K according to equation 1, for IAST calculations.

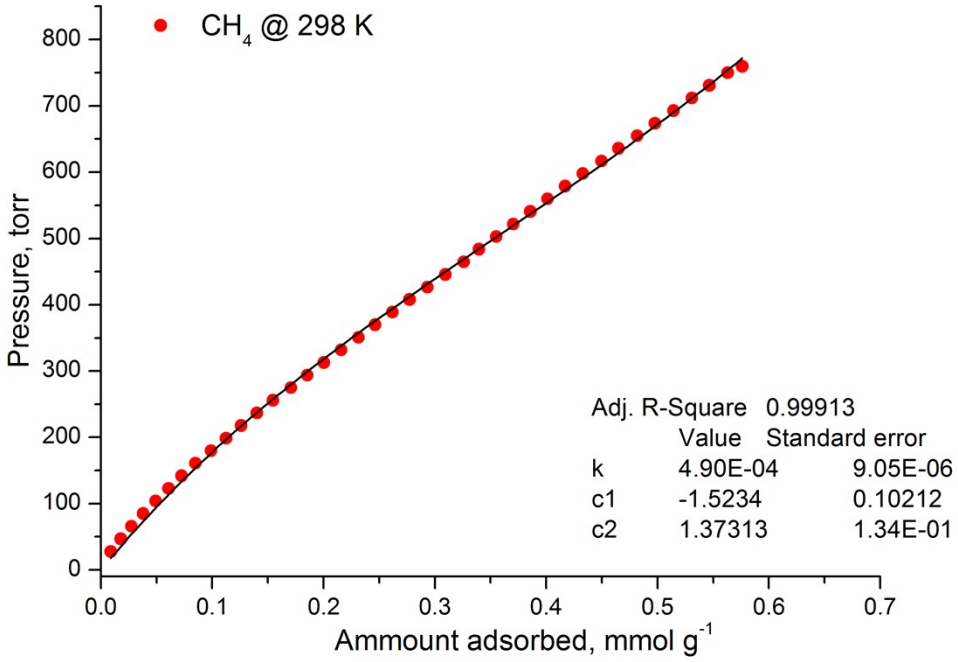

Figure S11. Virial type fitting of CH_4 adsorption isotherms of **1** at 298 K according to equation 1, for IAST calculations

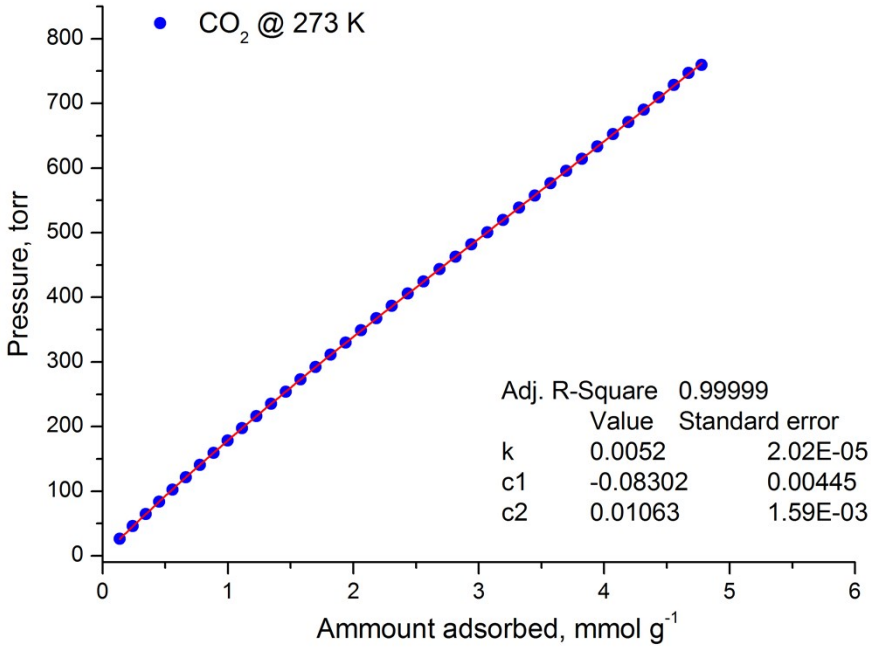

Figure S12. Virial type fitting of CO_2 adsorption isotherms of **1** at 273 K according to equation 1, for IAST calculations.

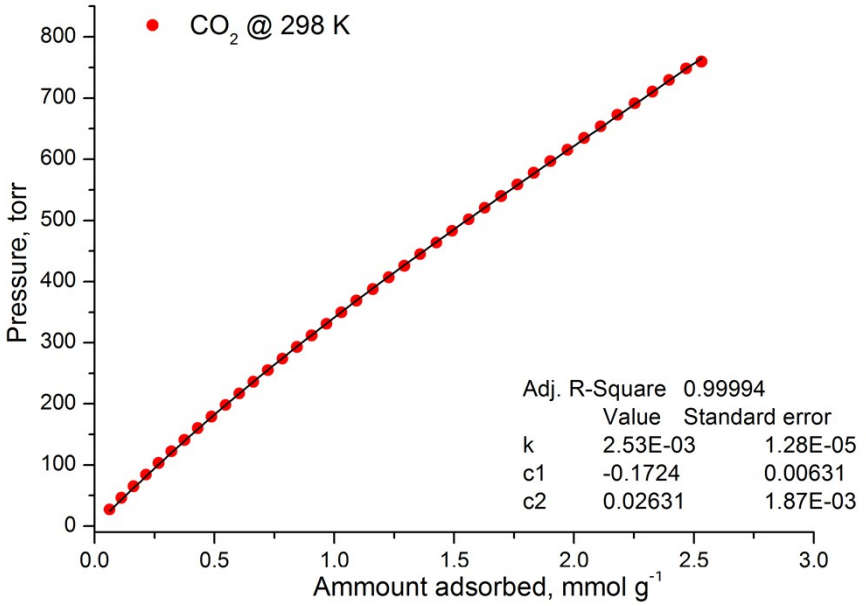

Figure S13. Virial type fitting of CO_2 adsorption isotherms of **1** at 298 K according to equation 1, for IAST calculations.

^{1}H NMR Spectra of acid digested samples

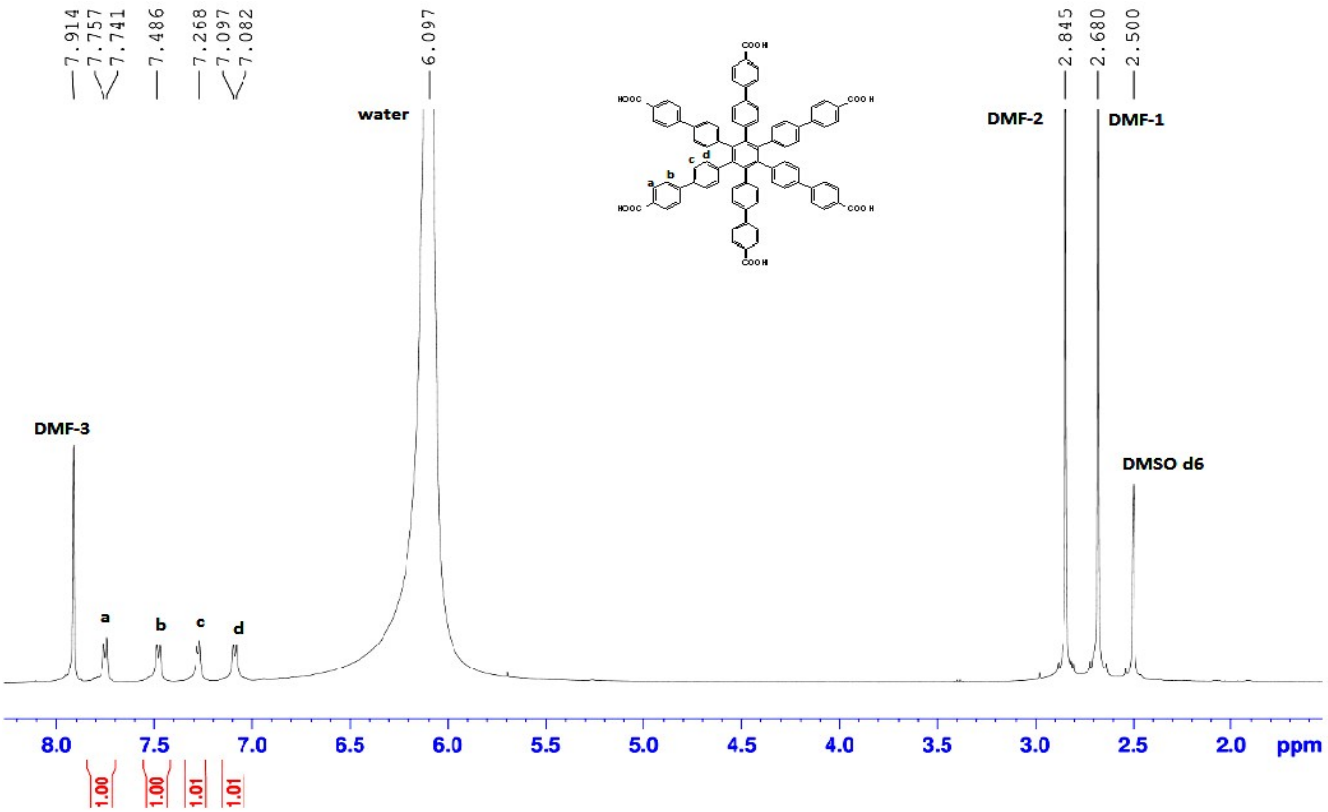

Figure S14. ^{1}H NMR spectrum of as-made **1** after digesting the sample in HCl/DMSO-*d*6 solution.

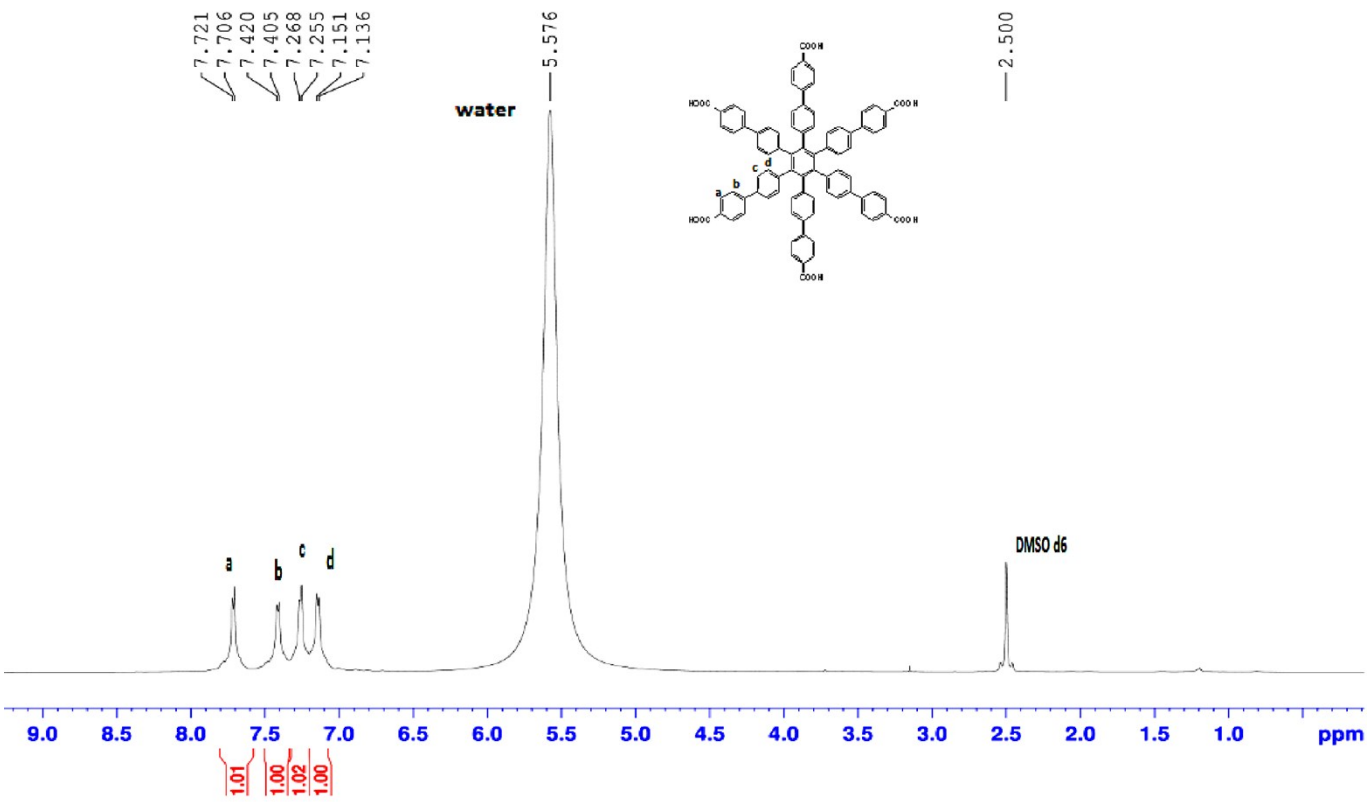

Figure S15. ^{1}H NMR spectrum of **1** after CO_2 supercritical drying and digesting the sample in HCl/DMSO-*d*6 solution. No residual solvents were observed.

Thermal gravimetric analyses (TGA)

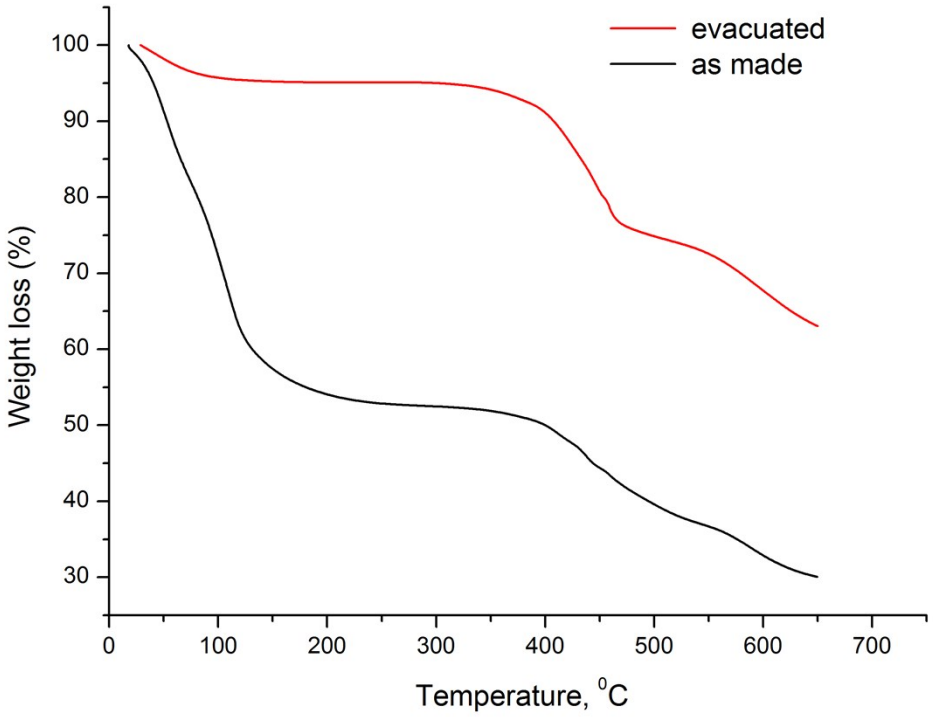

Figure S16. TGA curve for the as-made **1** (black line) and the corresponding evacuated solid (red line) obtained after CO_2 SCD process, recorded under N_2 flow with a heating rate of 5 deg/min.

Table S6. Comparison of **1** with selected MOFs in terms of BET surface area and CH_4 isosteric heat of adsorption.

Compound	**BET area** $m^2\ g^{-1}$	$\boldsymbol{Q_{st}^0}$ $kJ\ mol^{-1}$
1	1299	18.2
Cu-INIP[2]	1785	21.2
MAF-38[3]	2022	21.6
Ni-MOF-74[4]	1350	21.4
HKUST-1[6]	1850	17
PCN-14[6]	2000	18.7
UTSA-76[5]	2820	15.4
NU-111[6]	4930	14.2
NU-1100[7]	4020	13.7

Quantum chemistry calculations

Quantum chemistry calculations were performed in order to get further insight into the interaction of CO_2 and CH_4 with the structure of **1**. Two molecular models were constructed to represent the adsorption sites in **1** as shown in Figure S17. The first model is composed by a central phenyl ring together with six biphenyl arms. The second model contains the inorganic building block, $Co_2Cl(\text{-}COO)_3$, with the corresponding biphenyl arms and the octahedral Co^{2+} cation was terminated with three ethanol molecules, to avoid unrealistic calculations, despite the fact that the evacuated solid contains no solvent molecules. This because, a solvent free $Co_2Cl(\text{-}COO)_3$ cluster would have a 3-coordinated Co^{2+} with three unsaturated sites, which is not realistic. Although the structure of the evacuated solid is not known, given the high microporosity found experimentally (68% of the calculated value based on the crystal structure), it is suggested that upon removal of the solvent molecules, neighboring layers in **1** are shifted to each other, in order for the coordinated Cl^- anion from one layer to interact with the coordinatively unsaturated Co^{2+} of the next layer, making a pseudo-tetrahedral Co^{2+} atom and stabilize in this way the structure, see Figure S18. This kind of stabilization (shift of layers and stabilization of neighboring inorganic building units) is known in 2D MOFs, as for example in MOF-2.[8] Note that in the solvated, as-made **1**, the Cl…Co distance is small, ~6.3 Å, and a relative shift of ~2 Å for each layer in opposite direction, will create a new sort Cl…Co contact of <3Å (2.8 Å is shown in figure S18), and

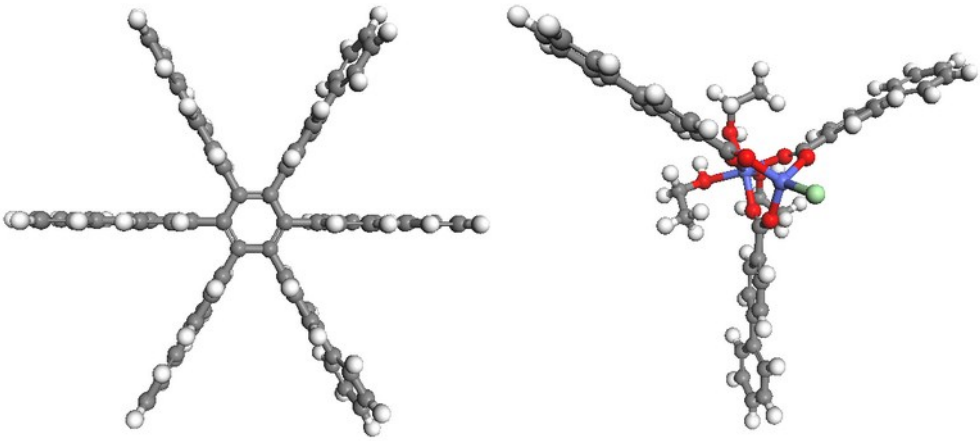

Figure S17. The two molecular models that were used to represent the binding sites of the MOF structure during calculations.

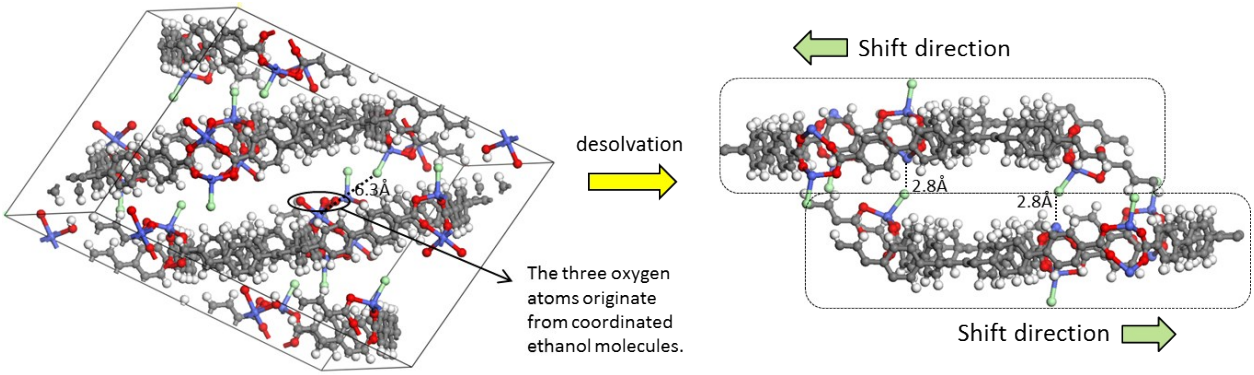

Figure S18. A proposed stabilization mechanism of desolvated **1**.

stabilize the solvent free Co^{2+} in a pseudo-tetrahedral coordination environment, see Figure S18. We decided not to perform the theoretical calculations in this structure, because the outcome could be sensitive to the relative shift of the layers (which is not known), making the results more complicated.

Both models were taken from the original crystal structure of **1** and the dangling bonds were saturated by adding hydrogen atoms. The positions of the atoms were kept fixed during calculations with the exception of the hydrogen and chlorine atoms, the ethanol molecules and the adsorbed guest molecules. The prediction of the geometry and the calculation of the interaction energies was based on the Density Functional Theory (DFT) method and the RI-PBE/def2-TZVP[9] computational model. Very tight convergence criteria were used for both the self-consistent field procedure (10^{-8} au) and the gradient (10^{-4} au). The corresponding auxiliary basis sets were used for the Resolution of Identity (RI) [10]approxi mation. The dispersion correction method of Grimme et al[11] with the proposed damping function of Becke-Johnson[12] was used to correct the total electronic energies due to the existence of dispersion forces. The calculation was performed with the Turbomole[13] quantum chemistry package.

The results that were obtained from the calculations show that CO_2 interacts stronger with the pore surface of **1**, compared to CH_4. For the molecular model in the left of figure S17, two binding sites were identified. The first is on top of the central phenyl ring of the ligand where the second is the pocket which is formed between two adjacent biphenyl arms. The calculated interaction energy over the central phenyl ring was found to be 15.9

kJ·mol^{-1} and 20.1 kJ·mol^{-1} for CH_4 and CO_2 respectively, where for the pocket site the corresponding calculated values were slightly higher at 17.6 kJ·mol^{-1} and 25.9 kJ·mol^{-1}. The distances of the carbon atoms of CH_4 and CO_2 from the center of the central phenyl ring are 3.6Å and 3.7Å. The corresponding distances from the two biphenyl arms forming the pocket site were measured to be 3.4Å and 3.5Å respectively. The optimized positions of the guest molecules can be seen in figure S19. For the case of the second molecular model that represents the inorganic building block in **1**, we found out that for both gases the strongest interaction site is the pocket formed between two adjacent biphenyl arms, as shown figure S20. The calculated interaction energies for this pocket were found to be 17.6 kJ·mol^{-1} and 26.3 kJ·mol^{-1} for CH_4 and CO_2 respectively. CO_2 is oriented almost parallel to a virtual axis that passes through the Cobalt atoms and both C-O bonds and the corresponding O-C-O angle were slightly more distorted than in case of the interaction with the two sites in first molecular model. In the case of CH_4, the molecule is oriented with the two of its hydrogen atoms looking towards the Cobalt atoms and it is located at a distance of 4Å far from the Cobalt atom connected to the chlorine atom.

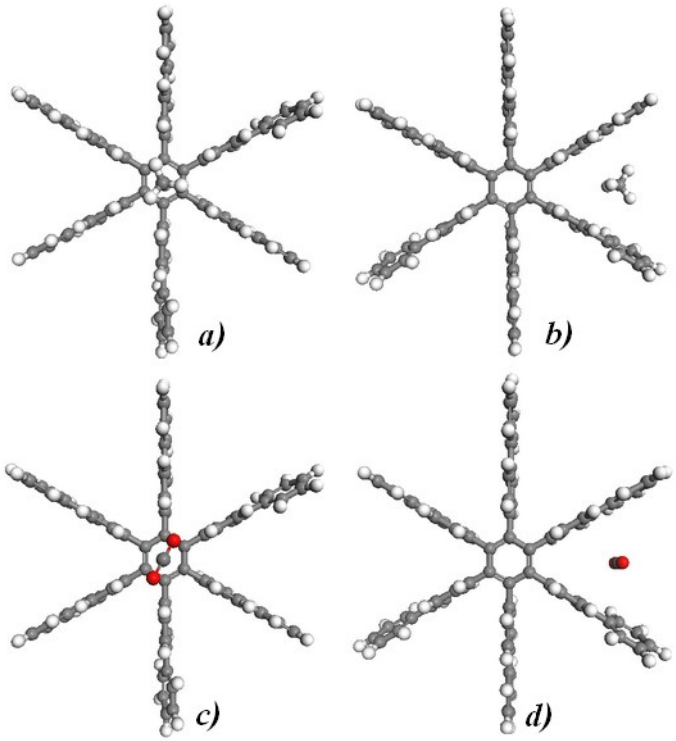

Figure S19. The optimized positions of the CH_4 (a,b) and CO_2 (c,d) molecules in the two binding sites found over the central phenyl ring and between two adjacent biphenyl arms.

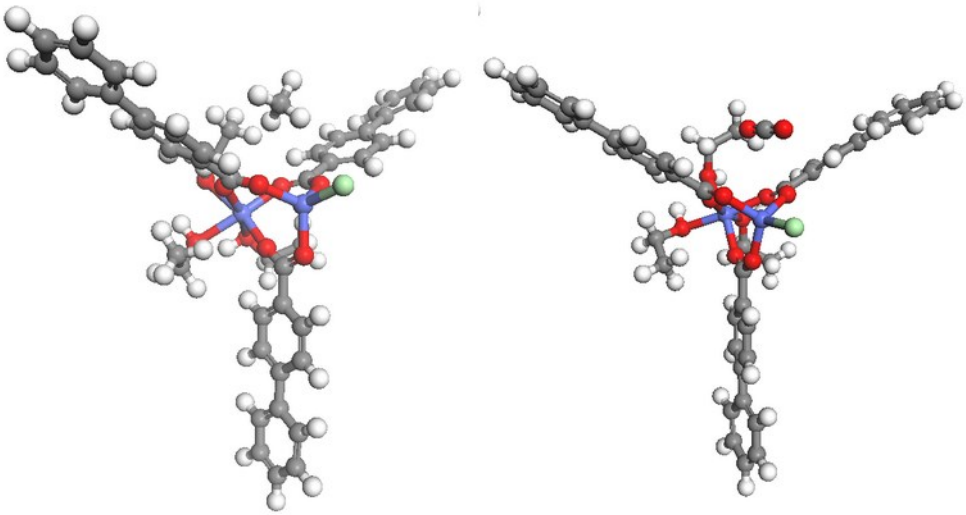

Figure S20. The optimized positions of the CH_4 (left) and CO_2 (right) molecules in the molecular model containing the inorganic building block.

References

[1] (a) Myers A. L., Prausnitz J. M., *AIChE J*., **1965**, 11, 121-127. (b) Bae Y., Mulfort K. L., Frost H., Ryan P., Punnathanam S., Broadbelt, L. J., Hupp J. T., Snurr R. Q., *Langmuir*, **2008**, 24, 8592-8598. (c) Armatas G.S., Kanatzidis M.G., *Nat. Mater*, **2009**, 8, 217-222.

[2] A. Kourtellaris, E. E. Moushi, I. Spanopoulos, C. Tampaxis, G. Charalambopoulou, T. A. Steriotis, G. S. Papaefstathiou, P. N. Trikalitis and A. J. Tasiopoulos, *Inorg. Chem. Front.*, **2016**, 3, 1527-1535.

[3] J. M. Lin, C. T. He, Y. Liu, P. Q. Liao, D. D. Zhou, J. P. Zhang and X. M. Chen, *Angew. Chem. Int. Ed.*, **2016**, 55, 4674-4678.

[4] Peng Y., Krungleviciute V., Eryazici I., Hupp J. T., Farha O. K., Yildirim T., *J. Am. Chem. Soc*., 135, **2013**, 11887-11894.

[5] Li B., Wen H., Wang H., Wu H., Tyagi M., Yildirim T., Zhou W., Chen B., *J. Am. Chem. Soc*.,136, **2014**, 6207-6210.

[6] Peng Y., Srinivas G., Wilmer C. E., Eryazici I., Snurr R.Q., Hupp J. T., Yildirim T., Farha O. K., *Chem. Commun*., **2013**, 49, 2992-2994.

[7] Gutov O. V., Bury W., Gomez-Gualdron D. A., Krungleviciute V., Fairen-Jimenez D., Mondloch J. E., Sarjeant A. A., Al-Juaid S. S., Snurr R. Q., Hupp J. T., Yildirim T., Farha O. K., *Chem. Eur. J.,* **2014**, 20, 12389-12393.

[8] H. Li, M. Eddaoudi, T. L. Groy, O. M. Yaghi, *J. Am. Chem. Soc.*, **1998**, *120*, 8571-8572.

[9] Weigend, F., Ahlrichs, R. *Phys. Chem. Chem. Phys*. 2005, 7, 3297.

[10] Weigend F., Häser, M. *Theor. Chem. Acc.* 1997, 97, 331.

[11] S. Grimme, J. Antony, S. Ehrlich, and S. Krieg, ``A consistent and accurate ab initio parametrization of density functional dispersion correction (dft-d) for the 94 elements H-Pu'', J. Chem. Phys. 2010, 132, 154104.

[12] S. Grimme, S. Ehrlich, and L. Goerigk, ``Effect of the damping function in dispersion corrected density functional theory'', J. Comp. Chem. 2011, 32, 1456.

[13] Ahlrichs, R., Bar, M., Haser, M., Horn, H., Kolmel, C. *Chem. Phys. Lett*. 1989, 162, 165−169.